

Local rheology relation with variable yield stress ratio across dry, wet, dense, and dilute granular flows

Thomas Pächtz^{1,2,*}, Orencio Durán³, David N. de Klerk^{4,5}, Indresan Govender⁶, and Martin Trulsson⁷

1. Institute of Port, Coastal and Offshore Engineering,
Ocean College, Zhejiang University, 310058 Hangzhou, China

2. State Key Laboratory of Satellite Ocean Environment Dynamics,
Second Institute of Oceanography, 310012 Hangzhou, China

3. Department of Ocean Engineering, Texas A&M University, College Station, Texas 77843-3136, USA

4. Centre for Minerals Research, University of Cape Town, Private Bag Rondebosch, 7701, South Africa

5. Department of Physics, University of Cape Town, Private Bag Rondebosch, 7701, South Africa

6. School of Engineering, University of KwaZulu-Natal, Glenwood, 4041, South Africa

7. Theoretical Chemistry, Department of Chemistry, Lund University, Lund, Sweden

Dry, wet, dense, and dilute granular flows have been previously considered fundamentally different and thus described by distinct, and in many cases incompatible, rheologies. We carry out extensive simulations of granular flows, including wet and dry conditions, various geometries and driving mechanisms (boundary-driven, fluid-driven, and gravity-driven), many of which are not captured by standard rheology models. For all simulated conditions, except for fluid-driven and gravity-driven flows close to the flow threshold, we find that the Mohr-Coulomb friction coefficient μ scales with the square root of the local Péclet number Pe provided that the particle diameter exceeds the particle mean free path. With decreasing Pe and granular temperature gradient M , this general scaling breaks down as weakening compressive stresses allow the mechanical stabilization of the flow. This leads to a yield condition with a variable yield stress ratio characterized by M .

Reliable large-scale simulations and thus predictions of geophysical and industrial processes require a deep understanding of the continuum properties of granular flows (i.e., the collective motion of granular particles). However, existing theories of the granular flow continuum (the “rheology”) are limited to small subsets of the physical conditions under which such processes can occur. For example, although geophysical granular flows are often wet (i.e., significantly affected or driven by ambient fluid) [1–3] and consist of coexisting dense (liquid-like) and dilute (gas-like) flow layers [3–7], even understanding comparably simple dry, dense-only or dilute-only flows has remained a major challenge [8–11].

Existing rheologies for noncohesive and nonquasistatic flows of sufficiently hard granular particles can be classified in terms of the particle volume fraction ϕ (the fraction of space covered by particles), particle-fluid-density ratio $s \equiv \rho_p/\rho_f$, and Stokes number $St \equiv \rho_p \dot{\gamma} d^2/\eta_f$, where d is the particle diameter, $\dot{\gamma}$ the granular shear rate, and η_f the fluid viscosity. Dilute, dry flows ($\phi \lesssim 0.5$, $s \rightarrow \infty$, $St \rightarrow \infty$) have been described by the kinetic theory of dry granular gases [12–15]; dense, dry flows ($\phi \gtrsim 0.5$, $s \rightarrow \infty$, $St \rightarrow \infty$) by the local viscoplastic rheology [16] and its nonlocal extensions [17–20]; dense solid-liquid suspensions ($\phi \gtrsim 0.5$, $s \simeq 1$, variable St) by different (partially incompatible [21]) viscoinertial rheologies [22–27]; and sediment transport driven by liquids (variable ϕ , $1 < s < 3$, variable St) by modified viscoplastic or viscoinertial rheologies [28–30]. Furthermore, different rather complex and controversial approaches exist to extend kinetic theory to solid-gas suspensions [31–33] or the dense regime [34–36].

Here we show that, despite their fundamental dif-

ferences, granular flows from the entire phase space (ϕ, s, St) actually obey a common scaling law for the Mohr-Coulomb friction coefficient μ , the knowledge of which is essential for any rheological description.

We carry out discrete element method-based simulations of granular flows for a variety of geometries and driving mechanisms (Table I and Fig. 1), which cover the entire phase space: (i) two-dimensional sediment transport driven by a large variety of Newtonian fluids, (ii) two-dimensional rapid gravity-driven flows in ambient static air of varying viscosity (including convective, “supported” flows [7]), (iii) two-dimensional uniformly sheared viscous suspensions in density-matched fluid of varying viscosity, (iv) two-dimensional dry uniform shear flows, (v) three-dimensional rotating drum flows lubricated by a density-matched fluid, and (vi) a three-dimensional dry rotating drum flow. Among these flows, convective gravity flows and rotating drum flows are known to elude the description by standard rheology models [4–7, 37, 38]. In all simulations, contacting particles interact via normal repulsion (restitution coefficient e , modeled through viscous damping), governed either by a linear or Hertzian law, and tangential friction (contact friction coefficient μ_c , Table I). Details are described below.

Sediment transport and gravity flows.—The numerical model couples a discrete element method for the particle motion (stiffness $k = 5000mg/d$) under gravity, buoyancy, and fluid drag with a continuum Reynolds-averaged description of hydrodynamics (described in detail and/or validated in Refs. [39–43]). Spherical particles ($\sim 10^4$) with mild polydispersity are confined in a quasi-two-dimensional, vertically infinite domain of length $\sim 10^3d$

Flow geometry	Driven by	Contact model (e, μ_c)
Sediment transport (2D)	Fluid	Linear (0.9, 0.5)
Rapid gravity flows (2D)	Gravity	Linear (0.9, 0.5)
Sheared suspensions (2D)	Boundary	Linear (0.1, 0.4)
Dry shear flows (2D)	Boundary	Linear (0.1, 0.4)
Lubricated drum flows (3D)	Boundary	Hertz (0.5, 0.5)
Dry drum flow (3D)	Boundary	Hertz (0.5, 0.5)

TABLE I. Summary of simulated granular flows.

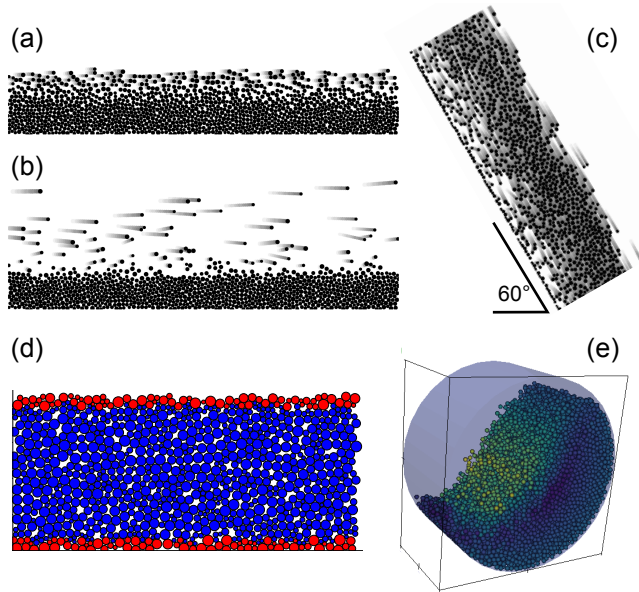


FIG. 1. Visualizations of numerical simulations of (a & b) sediment transport driven by various Newtonian fluids, (c) rapid, “supported” [7] gravity-driven flows in ambient static air, (d) uniformly sheared flows, and (e) rotating drum flows.

with periodic boundary conditions in the flow direction. The bottom-most particle layer is more dissipative and glued on a bottom wall. The Reynolds-Averaged Navier-Stokes equations are combined with an improved mixing length approximation, which can be used to calculate the mean turbulent fluid velocity at high particle concentrations. For gravity flows, the ambient fluid is kept static.

Simulations are carried out for varying density ratio s , Galileo number $\text{Ga} \equiv \rho_f \sqrt{(s-1)gd^3}/\eta_f$, Shields number $\Theta \equiv \tau_f/[(\rho_p - \rho_f)gd]$, and inclination angle α , where g is the gravitational constant and τ_f is the bed fluid shear stress. For gravity flows, we simulate conditions with $s = 2000$, $\text{Ga} \in [2, 100]$, $\Theta = 0$, and α between the flow threshold and 60° . For sediment transport, we simulate conditions with $s \in [2.65, 2000]$, $\text{Ga} \in [0.1, 100]$, $\alpha = 0$, and Θ above the flow threshold, which correspond to five different transport regimes (Table II) [42]. Following the symmetry along the flow direction, simulation data are averaged over horizontal layers of variable thickness depending on the particle volume fraction [39].

Sediment transport regime	Condition
Viscous bedload transport	$\sqrt{s}\text{Ga} < 20$
Turbulent bedload transport	$\sqrt{s}\text{Ga} \geq 20 \wedge s < 10$
Bedload-saltation transition	$20 \leq \sqrt{s}\text{Ga} < 80 \wedge s \geq 10$
Viscous saltation transport	$\sqrt{s}\text{Ga} \geq 80 \wedge s \geq 10 \wedge \sqrt[4]{s}\text{Ga} < 32$
Turbulent saltation transport	$\sqrt{s}\text{Ga} \geq 80 \wedge s \geq 10 \wedge \sqrt[4]{s}\text{Ga} \geq 32$

TABLE II. Sediment transport regimes [42].

Uniformly sheared particle and suspension flows.—The numerical model couples a discrete element method for the particle motion ($k = 2000P_{zz}d$) under viscous fluid drag and torque, with the Stokes equations for laminar flow (described in detail in Refs. [23, 44]). Two-dimensional disks ($\sim 10^3$) with moderate polydispersity are confined within a shear cell composed by two rough walls, created by gluing together two dense layers of grains, with periodic boundary conditions along the flow direction parallel to the walls. The position of the walls is controlled to ensure constant confining pressure P_{zz} and mean shear rate.

Simulations are carried out for varying volume fraction (in the range $\phi > 0.24$, where ϕ is calculated as $2/3$ of the disk area fraction, like for spheres confined in two dimensions) and two general cases: no ambient fluid (dry condition) and an ambient density-matched liquid with varying dimensionless viscosity ($s = 1, \eta_f/\sqrt{\rho_p P_{zz}d^2} = [10^{-3}, 10^{-2}, 10^{-1}, 10^0, \infty]$). Simulation data are averaged over the entire shear cell.

Rotating drum flows.—The numerical model uses a discrete element method for the particle motion ($k = 17000mg/d^{3/2}$) under lubrication forces [24] and gravity. The contact model employs the LIGGGHTS implementation of Hertzian contacts, which ensures a constant value of e [45, 46]. Spherical monodisperse particles ($\sim 10^4$) are confined within a closed horizontal cylinder (drum) of radius $20d$ and width $20d$ rotating at a constant rate ω .

Simulations are carried out for no ambient fluid (dry condition) and an ambient density-matched liquid with varying dimensionless viscosity ($s = 1, \eta_f/(\rho_f \omega d^2) = [1/160, 1/16, 3/16]$). Simulation data are averaged using an anisotropic Gaussian smoothing function of dimension $3d \times 3d \times 20d$.

General rheology relation.—Contact (\mathbf{P}^c) and kinetic (\mathbf{P}^k) granular stresses are calculated from the simulation data using the method given in Ref. [48], which ensures that the granular temperature $T = \sum_i P_{ii}^k/(\rho_p \phi D)$ (the root-mean-square of the particle fluctuation velocity), where D is the number of space dimensions, is insensitive to the coarse-graining width. Furthermore, the shear rate $\dot{\gamma}$ is calculated as the norm of the deviatoric component of the strain rate tensor $\epsilon_{ij} \equiv \partial_i \langle v_j \rangle + \partial_j \langle v_i \rangle$,

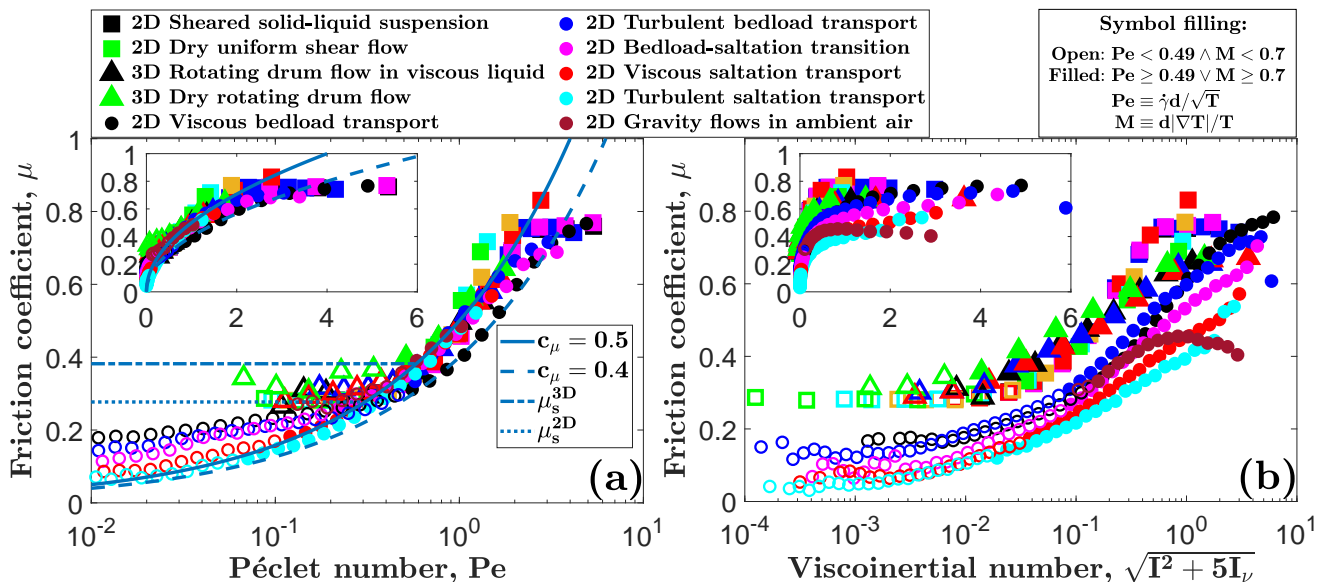


FIG. 2. Mohr-Coulomb friction coefficient μ vs (a) Péclet number Pe and (b) viscoinertial number $K \equiv \sqrt{I^2 + 5I_\nu}$ for data from discrete element method-based simulations of various granular flows. The values of Pe , K , and μ depend on the location within the flow. The value of μ at each location with $\lambda(\phi) < d$ and either $Pe < 0.49 \wedge M < 0.7$ (open symbols) or $Pe \geq 0.49 \vee M \geq 0.7$ (filled symbols) is allocated to the corresponding bin of Pe or K . Each bin consists of data from either a single simulation (rotating drum and uniform flows) or from various simulations of the same regime (sediment transport and gravity flows, see Tables II and S1). The mean of μ within each bin is represented by the symbols (for standard deviation, see Fig. S2). For the squares, the color order (green, cyan, orange, red, magenta, blue, black) corresponds to $\eta_f/\sqrt{\rho_p P_{zz} d^2} = [0, 10^{-3}, 10^{-2}, 10^{-1}, 10^0, 10^1, \infty]$. For the triangles, the color order (green, red, blue, black) corresponds to $\eta_f/(\rho_f \omega d^2) = [0, 1/160, 1/16, 3/16]$.

which reads $\dot{\gamma} \equiv \|\epsilon^d\| = \sqrt{\sum_{ij} \epsilon_{ij}^d \epsilon_{ij}^d / 2}$, where $\epsilon_{ij}^d = \epsilon_{ij} - \sum_k \epsilon_{kk} \delta_{ij} / D$. Finally, we calculate the Mohr-Coulomb friction coefficient $\mu \equiv \max_{i,j} |P_i^c - P_j^c| / |P_i^c + P_j^c|$ from the principal components P_i^c of \mathbf{P}^c (a Drucker-Prager definition of μ and/or a definition that includes kinetic stresses yield slightly but statistically significantly worse results).

For both dilute and dense flow conditions (defined shortly), we find that the friction coefficient μ is only a function of the Péclet number $Pe \equiv \dot{\gamma}d/\sqrt{T}$ [34] and scales as

$$\mu = c_\mu \sqrt{Pe}, \quad (1)$$

almost everywhere within all simulated conditions (Fig. 2a, filled symbols), except for sediment transport and gravity flows too close to the flow threshold (which are excluded from Fig. 2) because of nonlocal effects (see supplementary materials for details [49]). The scale parameter c_μ slightly depends on the driving conditions, with the smallest value found for viscous bedload transport. For uniformly sheared flows, c_μ varies significantly with the contact friction coefficient ($c_\mu \simeq 0.3$ for $\mu_c = 0$, $c_\mu \simeq 0.55$ for $\mu_c = 100$) but not with the normal restitution coefficient e , even in the extreme cases $\mu_c = 100$ (no sliding) and $\mu_c = 0$ (always sliding) [49]. We there-

fore propose that Eq. (1) relates the structure anisotropy to μ , where c_μ partly encodes the anisotropy of the tangential contact force network (which increases with μ_c) and Pe encodes the anisotropy of the particle assembly (i.e., the unit normal contact vector), relating the diffusion forces toward isotropic configurations to that of the anisotropic compression and extension of the shear [34]. This proposition is consistent with dry uniform shear flows, for which both anisotropies correlate with μ [50]. Alternatively, Pe may also be interpreted as the ratio between the rates of the macroscopic shearing motion ($\dot{\gamma}$) and microscopic kinetic rearrangements ($\propto \sqrt{T}/d$), which is similar to the original interpretations of the inertial number $I = \dot{\gamma}d/\sqrt{P^c/\rho_p}$ (where $P^c \equiv \sum_i P_{ii}^c/D$) and viscous number $I_\nu \equiv \eta_f \dot{\gamma} / P^c$ [51]. The difference is that, for I (and I_ν), the kinetic rearrangement rate has been obtained from assuming a particle fall driven by pressure (and opposed by viscous drag), whereas for Pe , the kinetic rearrangement rate is obtained from the actual relative motion between neighboring particles. The latter rate should be more general, which is supported by the fact that, in contrast to Pe , neither I (even when limited to dry flows), nor I_ν , nor a combination of the two collapse the μ data (Fig. 2b and supplementary materials [49]), except the viscoinertial number $\sqrt{I^2 + 5I_\nu}$ for uniform flows (Fig. 2b). Note that a standard nonlo-

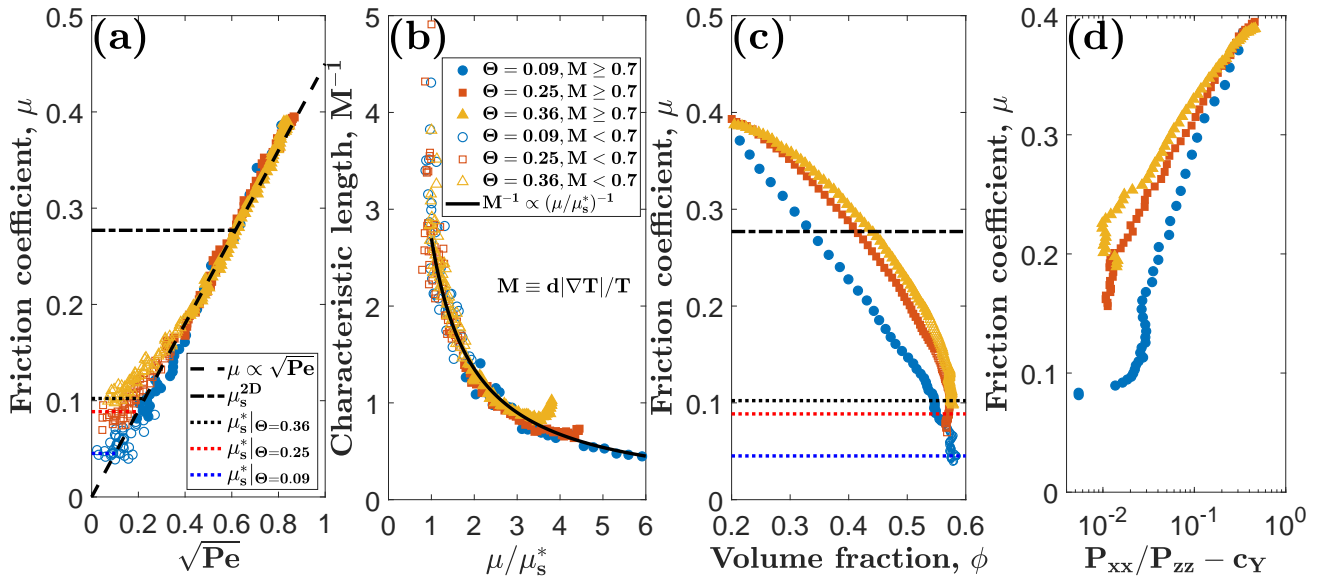


FIG. 3. (a) Mohr-Coulomb friction coefficient μ vs square root of Péclet number ($\sqrt{\text{Pe}}$). (b) Characteristic length M^{-1} vs rescaled friction coefficient μ/μ_s^* . (c) μ vs particle volume fraction ϕ . (d) μ vs $P_{xx}/P_{zz} - c_Y$, where $\mathbf{P} = \mathbf{P}^c + \mathbf{P}^k$ and $c_Y = 0.98 \neq 1$ because finite-size effects allow for slight normal stress differences at yielding [47]. Symbols correspond to data with $\lambda(\phi) < d$ from simulations of turbulent saltation transport ($s = 2000$, $\text{Ga} = 5$) for three different Shields numbers Θ . Filled symbols indicate $\text{Pe} \geq 0.49 \vee M \geq 0.7$. Open symbols indicate $\text{Pe} < 0.49 \wedge M < 0.7$ [not shown in (d) for visibility reasons].

cal rheology model [17, 20] and extended kinetic theory also fail to describe our flows [49]. In particular, the latter predicts $\mu \simeq c_\mu^{\text{kin}} \text{Pe}$ for dense flows [34, 36] (with a proportionality constant c_μ^{kin} that depends on e but not on μ_c), inconsistent with Eq. (1) and our data.

We define dilute and dense conditions – as opposed to rarefied ones – in terms of the mean free path λ through the condition $\lambda < d$, where $\lambda(\phi) = \sqrt{2}d/(12\phi)$ for spherical particles and $\lambda(\phi) = \pi d/(12\sqrt{2}\phi)$ for spheres confined in two dimensions. In fact, we hypothesize that at least some of the few deviations from the scaling in Eq. (1) at large Pe (Fig. 2a) are related to a transition from dilute to rarefied flows at large shear rates, where μ is limited by the geometrical constraints of high energy collisions [43].

Variable yield stress ratio.—Interestingly, deviations from the scaling in Eq. (1) at small Pe (larger-than-predicted values of μ) are well characterized by the dimensionless granular temperature gradient $M \equiv d|\nabla T|/T$ and seem to occur whenever $M \lesssim 0.7$ and $\text{Pe} \lesssim 0.5$ (Fig. 2a, open symbols). For shear rate and pressure-controlled homogeneous flows (e.g., uniform shear, squares in Fig. 2), where temperature gradients are negligible ($M \sim 0$), these deviations are owed to the fact that μ converges to the yield stress ratio μ_s ($\mu_s^{2D} = 0.277$ [23], $\mu_s^{3D} = 0.382$ [34]) in the limit of vanishing shear rate. From Eq. (1), we find that this yield transition in homogeneous flows starts at $\text{Pe} = (\mu_s/c_\mu)^2 \approx 0.5$.

For inhomogeneous flows, like sediment transport, the

friction coefficient μ can be substantially smaller than μ_s when $\text{Pe} \lesssim 0.5$ (Figs. 2a and 3a), at which point deviations from the scaling in Eq. (1) are controlled by temperature gradients, in particular the condition $M \lesssim 0.7$. These deviations have several elements in common with a yield transition, as illustrated in Fig. 3 for turbulent saltation transport, which is a nearly dry granular flow because of a large density ratio ($s = 2000$) and large Stokes numbers [$\text{St} \in (10, 200)$]. First, μ seems to converge to a finite value μ_s^* in the limit of vanishing shear rate (Fig. 3a). Second, the dimensionless characteristic length M^{-1} , associated with spatial changes in the granular temperature, collapses as a function of μ/μ_s^* with a peak at $\mu/\mu_s^* = 1$ (Fig. 3b). This peak is reminiscent of the divergence of the relaxation length associated with spatial changes of the shear rate ($\dot{\gamma}$) and granular stresses (\mathbf{P}^c) when approaching the yield condition ($\mu \rightarrow \mu_s$) in existing nonlocal rheology models [19]. Finally, ϕ approaches the packing fraction as $\mu \rightarrow \mu_s^*$ (Fig. 3c). We thus conclude that μ_s^* is the analogue of μ_s for inhomogeneous flows.

The onset of the yield transition is thus a function of the dimensionless temperature gradient M and Péclet number Pe . This can be explained under the assumption that, like in dilute flows [12–14], both velocity and temperature gradients generate normal stress differences, which are associated with compressive stresses. In fact, because the yielding transition is characterized by vanishing normal stress differences ($P_{xx}/P_{zz} - 1 = 0$) in the

large-system limit [47] (Fig. 3d), larger values of M shift the yielding transition to smaller values of Pe and thus μ via Eq. (1). Note that, for inhomogeneous flows, general local relationships, like Eq. (1), are not expected to work at locations that exhibit a sub-critical stress ratio ($\mu < \mu_s$) [19].

Conclusions.—In this study, we have shown that, under certain relatively weak constraints, the Mohr-Coulomb friction coefficient μ obeys the general scaling $\mu = c_\mu \sqrt{Pe}$, with the Péclet number defined as $Pe \equiv \dot{\gamma}d/\sqrt{T}$ (but, in general, disobeys scaling laws from visco-inertial rheology models and extended kinetic theory). This calls for the development of hydrodynamic models for dense granular flows involving granular temperature. Apart from extended kinetic theory, several such models have already been proposed to reproduce several aspects such as hysteresis [52, 53] and drag on an object [54]. The scaling parameter c_μ varies with the tangential friction coefficient μ_c but not with the normal coefficient of restitution e , which led us to propose that $\mu = c_\mu \sqrt{Pe}$ encodes the effects of the anisotropies of the particle assembly (Pe) and tangential contact force network (c_μ) on μ .

The yield stress ratio of granular media, below which granular flows either stop or fundamentally change [19], is often found to be independent of the flow geometry [47]. However, for wind-driven sediment transport, the scaling $\mu \propto \sqrt{Pe}$ even holds for friction coefficients as low as $\mu \simeq 0.08$ and is accompanied by very low yield stress ratios (as low as $\mu_s^* \simeq 0.04$, reminiscent of vibrated granular flows [55]), which seem to be caused by additional compressive stresses generated by relatively large values of the dimensionless temperature gradient $M \equiv d|\nabla T|/T$. Future studies should investigate this link between μ_s^* and T because it may play a role in explaining long-standing open problems, such as the reduction of friction in long-runout landslides [56–58].

Thomas Pätz acknowledges support from grant National Natural Science Foundation of China (No. 11750410687). Martin Trulsson acknowledges funding from the Swedish Research Council (621-2014-4387). Simulations of rotating drums were performed using facilities provided by the University of Cape Town’s ICTS High-Performance Computing team (<http://hpc.uct.ac.za>). The DEM simulations of uniform flows were performed on resources provided by the Swedish National Infrastructure for Computing (SNIC) at the centre for scientific and technical computing at Lund University (LUNARC).

SUPPLEMENTARY MATERIALS

NONLOCALITY IN SEDIMENT TRANSPORT AND GRAVITY FLOWS

When the dimensionless fluid shear stress (“Shields number”) Θ of the fluid driving sediment transport is too close to its value at the flow threshold or when the inclination angle α of the gravity flows in ambient air is too close to its value at the flow threshold, the simulation data do not obey the scaling $\mu \propto \sqrt{Pe}$ (Fig. S1), which relates the local friction coefficient μ to the local Péclet number Pe (i.e., the granular flow rheology is nonlocal). This finding is not surprising because nonlocal effects are already known to be crucial for dry gravity flows (e.g., they are responsible for the stopping angle dependency on the flow thickness [19]) and because it is already known that sediment transport tends to creep below the surface of the granular bed [28], which is also associated with nonlocality [19]. In particular, for turbulent saltation transport, the granular bed does not flow liquidlike but creeps even relatively far from the flow threshold because the fluid shear stress at the bed surface is insufficient to mobilize particles [59]. Only for sufficiently intense conditions (i.e., those in Table S1), when collisions between particles of the rarefied transport layer and granular bed are so frequent that the bed no longer recovers between collisions, does the granular bed flow like a liquid and thus the rheology become local [43].

ALTERNATIVE MANNER TO EVALUATE THE PÉCLET NUMBER SCALING

Figure S2 shows the scaling $\mu = c_\mu \sqrt{Pe}$ for the same data as in Fig. 2a of the paper, but including the standard deviation for all our simulated flows (for uniform flows, it is usually smaller than the symbol size and therefore not shown).

INFLUENCE OF CONTACT PARAMETERS ON SCALING LAW

Figure S3 shows the influence of contact parameters on the scaling $\mu = c_\mu \sqrt{Pe}$ for uniformly sheared particle and suspension flows. It can be seen that the normal restitution coefficient e does not affect the scaling parameter c_μ . In contrast, c_μ increases with the contact friction coefficient μ_c .

FAILURE OF STANDARD RHEOLOGY MODELS

Failure of viscoplastic rheology and fluidity scaling

The viscoplastic $\mu(I)$ rheology predicts that there is a general relationship between the friction coefficient μ and the inertial number I across dense, dry granular flows [16]. However, Figs. S4a and S5a show that this prediction fails for our simulated nearly dry flows. This failure cannot be remedied by nonlocal extensions of the $\mu(I)$ rheology. For example, it has been demonstrated that the nonlocal model of Ref. [17] is based on a general scaling of the rescaled fluidity $\dot{\gamma}d/(\mu\sqrt{T})$ with the particle volume fraction ϕ [20], which is disobeyed across our dry flows (Fig. S5b).

Failure of viscoinertial rheology models

Figures S4b and S6b show that the failure of the $\mu(I)$ (Figs. S4a, S5a, and S6a) also cannot be remedied by the viscous number rheology $\mu(I_\nu)$ [22]. Interestingly, turbulent saltation transport roughly obeys the same power law with the viscoinertial number $\sqrt{I^2 + 5I_\nu}$ as uniformly sheared particle and suspension flows [$\mu \propto (I^2 + 5I_\nu)^{0.15}$], but the proportionality constant is much smaller (Fig. S6c).

Failure of extended kinetic theory

Extended kinetic theory predicts that the particle shear stress $\|\tau^c\| \equiv |P_1^c - P_2^c|/2$ (for two-dimensional flows), rescaled by $\rho_p d\sqrt{T}\dot{\gamma}$, and the rescaled particle pressure $P^c/(\rho_p T)$ are functions of only the particle volume fraction ϕ . However, it is well known that this prediction, in general, does not hold for wet granular flows [31–33], which is shown in Fig. S7 for uniformly sheared particle and suspension flows.

* 0012136@zju.edu.cn

- [1] S. Courrech du Pont, P. Gondret, B. Perrin, and M. Rabaud, “Granular avalanches in fluids,” *Physical Review Letters* **90**, 044301 (2003).
- [2] M. Houssais and D. J. Jerolmack, “Toward a unifying constitutive relation for sediment transport across environments,” *Geomorphology* **277**, 251–264 (2017).
- [3] R. Delannay, A. Valance, A. Mangeney, O. Roche, and P. Richard, “Granular and particle-laden flows: from laboratory experiments to field observations,” *Journal of Physics D: Applied Physics* **50**, 053001 (2017).
- [4] T. Börzsönyi, R. E. Ecke, and J. N. McElwaine, “Patterns in flowing sand: Understanding the physics of granular flow,” *Physical Review Letters* **103**, 178302 (2009).

- [5] A. J. Holyoake and J. N. McElwaine, “High-speed granular chute flows,” *Journal of Fluid Mechanics* **710**, 35–71 (2012).
- [6] N. Brodu, P. Richard, and R. Delannay, “Shallow granular flows down flat frictional channels: Steady flows and longitudinal vortices,” *Physical Review E* **87**, 022202 (2013).
- [7] N. Brodu, R. Delannay, A. Valance, and P. Richard, “New patterns in high-speed granular flows,” *Journal of Fluid Mechanics* **769**, 218–228 (2015).
- [8] GDR MiDi, “On dense granular flows,” *The European Physical Journal E* **14**, 341–365 (2004).
- [9] B. Andreotti, Y. Forterre, and O. Pouliquen, *Granular Media: Between Fluid and Solid* (Cambridge University Press, Cambridge, 2013).
- [10] P. Jop, “Rheological properties of dense granular flows,” *Comptes Rendus Physique* **16**, 62–72 (2015).
- [11] V. Kumaran, “Kinetic theory for sheared granular flows,” *Comptes Rendus Physique* **16**, 51–61 (2015).
- [12] N. Sela and I. Goldhirsch, “Hydrodynamic equations for rapid flows of smooth inelastic spheres, to burnett order,” *Journal of Fluid Mechanics* **361**, 41–74 (1998).
- [13] S. Saha and M. Alam, “Non-newtonian stress, collisional dissipation and heat flux in the shear flow of inelastic disks: a reduction via grad’s moment method,” *Journal of Fluid Mechanics* **757**, 251–296 (2014).
- [14] S. Saha and M. Alam, “Normal stress differences, their origin and constitutive relations for a sheared granular fluid,” *Journal of Fluid Mechanics* **795**, 549–580 (2016).
- [15] V. Garzó and J. W. Dufty, “Dense fluid transport for inelastic hard spheres,” *Physical Review E* **59**, 5895–5911 (1999).
- [16] P. Jop, Y. Forterre, and O. Pouliquen, “A constitutive law for dense granular flows,” *Nature* **441**, 727–730 (2006).
- [17] K. Kamrin and G. Koval, “Nonlocal constitutive relation for steady granular flow,” *Physical Review Letters* **108**, 178301 (2012).
- [18] M. Bouzid, M. Trulsson, P. Claudin, E. Clément, and B. Andreotti, “Nonlocal rheology of granular flows across yield conditions,” *Physical Review Letters* **111**, 238301 (2013).
- [19] M. Bouzid, A. Izzet, M. Trulsson, E. Clément, P. Claudin, and B. Andreotti, “Non-local rheology in dense granular flows – Revisiting the concept of fluidity,” *The European Physics Journal E* **38**, 125 (2015).
- [20] Q. Zhang and K. Kamrin, “Microscopic description of the granular fluidity field in nonlocal flow modeling,” *Physical Review Letters* **118**, 058001 (2017).
- [21] É. Guazzelli and O. Pouliquen, “Rheology of dense granular suspensions,” *Journal of Fluid Mechanics* **852**, P1 (2018).
- [22] F. Boyer, É. Guazzelli, and O. Pouliquen, “Unifying suspension and granular rheology,” *Physical Review Letters* **107**, 188301 (2011).
- [23] M. Trulsson, B. Andreotti, and Philippe Claudin, “Transition from the viscous to inertial regime in dense suspensions,” *Physical Review Letters* **109**, 118305 (2012).
- [24] C. Ness and J. Sun, “Flow regime transitions in dense non-Brownian suspensions: Rheology, microstructural characterization, and constitutive modeling,” *Physical Review E* **91**, 012201 (2015).

- [25] C. Ness and J. Sun, “Shear thickening regimes of dense non-Brownian suspensions,” *Soft Matter* **12**, 914–924 (2016).
- [26] L. Amarsid, J.-Y. Delenne, P. Mutabaruka, Y. Monerie, F. Perales, and F. Radjai, “Viscoinertial regime of immersed granular flows,” *Physical Review E* **96**, 012901 (2017).
- [27] E. DeGiuli, G. Düring, E. Lerner, and M. Wyart, “Unified theory of inertial granular flows and non-brownian suspensions,” *Physical Review E* **91**, 062206 (2015).
- [28] M. Houssais, C. P. Ortiz, D. J. Durian, and D. J. Jerolmack, “Onset of sediment transport is a continuous transition driven by fluid shear and granular creep,” *Nature Communications* **6**, 6527 (2015).
- [29] M. Houssais, C. P. Ortiz, D. J. Durian, and D. J. Jerolmack, “Rheology of sediment transported by a laminar flow,” *Physical Review E* **94**, 062609 (2016).
- [30] R. Maurin, J. Chauchat, and P. Frey, “Dense granular flow rheology in turbulent bedload transport,” *Journal of Fluid Mechanics* **804**, 490–512 (2016).
- [31] V. Garzó, S. Tenneti, S. Subramaniam, and C. M. Hrenya, “Enskog kinetic theory for monodisperse gassolid flows,” *Journal of Fluid Mechanics* **712**, 129–168 (2012).
- [32] M. G. Chamorro, F. Vega Reyes, and V. Garzó, “Revisiting ignited-quenched transition and the non-newtonian rheology of a sheared dilute gas-solid suspension,” *Physical Review E* **92**, 052205 (2015).
- [33] S. Saha and M. Alam, “Revisiting ignited-quenched transition and the non-newtonian rheology of a sheared dilute gas-solid suspension,” *Journal of Fluid Mechanics* **833**, 206–246 (2017).
- [34] S. Chialvo and S. Sundaresan, “A modified kinetic theory for frictional granular flows in dense and dilute regimes,” *Physics of Fluids* **25**, 070603 (2013).
- [35] D. Vescovi, D. Berzi, P. Richard, and N. Brodu, “Plane shear flows of frictionless spheres: Kinetic theory and 3d soft-sphere discrete element method simulations,” *Physics of Fluids* **26**, 053305 (2014).
- [36] D. Berzi and D. Vescovi, “Different singularities in the functions of extended kinetic theory at the origin of the yield stress in granular flows,” *Physics of Fluids* **27**, 013302 (2015).
- [37] P.-P. Cortet, D. Bonamy, F. Daviaud, O. Dauchot, B. Dubrulle, and M. Renouf, “Relevance of visco-plastic theory in a multi-directional inhomogeneous granular flow,” *Europhysics Letters* **88**, 14001 (2009).
- [38] I. Govender, “Granular flows in rotating drums: A rheological perspective,” *Minerals Engineering* **92**, 168–175 (2016).
- [39] O. Durán, B. Andreotti, and P. Claudin, “Numerical simulation of turbulent sediment transport, from bed load to saltation,” *Physics of Fluids* **24**, 103306 (2012).
- [40] O. Durán, P. Claudin, and B. Andreotti, “Direct numerical simulations of aeolian sand ripples,” *Proceedings of the National Academy of Science* **111**, 15665–15668 (2014).
- [41] T. Pähz and O. Durán, “Fluid forces or impacts: What governs the entrainment of soil particles in sediment transport mediated by a Newtonian fluid?” *Physical Review Fluids* **2**, 074303 (2017).
- [42] T. Pähz and O. Durán, “The cessation threshold of non-suspended sediment transport across aeolian and fluvial environments,” *Journal of Geophysical Research: Earth Surface* **123**, 1638–1666 (2018).
- [43] T. Pähz and O. Durán, “Universal friction law at granular solid-gas transition explains scaling of sediment transport load with excess fluid shear stress,” *Physical Review Fluids* **3**, 104302 (2018).
- [44] M. Trulsson, E. DeGiuli, and M. Wyart, “Effect of friction on dense suspension flows of hard particles,” *Physical Review E* **95**, 012605 (2017).
- [45] A. Di Renzo and F. Di Maio, “Comparison of contact-force models for the simulation of collisions in DEM-based granular flow codes,” *Chemical Engineering Science* **59**, 525–541 (2004).
- [46] A. Di Renzo and F. Di Maio, “An improved integral non-linear model for the contact of particles in distinct element simulations,” *Chemical Engineering Science* **60**, 1303–1312 (2005).
- [47] A. H. Clark, J. D. Thompson, M. D. Shattuck, N. T. Ouellette, and C. S. O’Hern, “Critical scaling near the yielding transition in granular media,” *Physical Review E* **97**, 062901 (2018).
- [48] R. Artoni and P. Richard, “Average balance equations, scale dependence, and energy cascade for granular materials,” *Physical Review E* **91**, 032202 (2015).
- [49] See Supplementary Material for nonlocal effects in gravity flows and sediment transport and for variance of c_μ with contact parameters.
- [50] E. Azéma and F. Radjaï, “Internal structure of inertial granular flows,” *Physical Review Letters* **112**, 078001 (2014).
- [51] C. Cassar, M. Nicolas, and O. Pouliquen, “Submarine granular flows down inclined planes,” *Physics of Fluids* **17**, 103301 (2005).
- [52] C.-H. Lee and C.-J. Huang, “Kinetic-theory-based model of dense granular flows down inclined planes,” *Physics of Fluids* **24**, 073303 (2012).
- [53] E. DeGiuli and M. Wyart, “Friction law and hysteresis in granular materials,” *Proceedings of the National Academy of Science* **114**, 9284–9289 (2017).
- [54] A. Seguin, Y. Bertho, P. Gondret, and J. Crassous, “Dense granular flow around a penetrating object: Experiment and hydrodynamic model,” *Physical Review Letters* **107**, 048001 (2011).
- [55] N. Gaudel and S. K. De Richter, “Effect of vibrations on granular material flows down an inclined plane using dem simulations,” *Powder Technology* **346**, 256–264 (2019).
- [56] F. Legros, “The mobility of long-runout landslides,” *Engineering Geology* **63**, 301–331 (2002).
- [57] A. Lucas, A. Mangeney, and J. P. Ampuero, “Frictional velocity-weakening in landslides on earth and on other planetary bodies,” *Nature Communications* **5**, 3417 (2014).
- [58] B. C. Johnson, C. S. Campbell, and H. J. Melosh, “The reduction of friction in long runout landslides as an emergent phenomenon,” *Journal of Geophysical Research: Earth Surface* **121**, 881–889 (2016).
- [59] O. Durán, P. Claudin, and B. Andreotti, “On aeolian transport: Grain-scale interactions, dynamical mechanisms and scaling laws,” *Aeolian Research* **3**, 243–270 (2011).

Category	Density ratio s	Galileo number Ga	Range of $\sqrt{\Theta}$ or α	# of simulations
Viscous bedload transport	2.65	2	$\sqrt{\Theta} \in [0.79, 1.39]$	11
Viscous bedload transport	2.65	5	$\sqrt{\Theta} \in [0.73, 1.18]$	10
Viscous bedload transport	2.65	10	$\sqrt{\Theta} \in [0.77, 1.12]$	8
Viscous bedload transport	100	0.5	$\sqrt{\Theta} \in [0.84, 1.02]$	4
Viscous bedload transport	2000	0.1	$\sqrt{\Theta} \in [0.84, 1.05]$	4
Turbulent bedload transport	2.65	20	$\sqrt{\Theta} \in [0.67, 0.91]$	7
Turbulent bedload transport	2.65	50	$\sqrt{\Theta} \in [0.61, 1.45]$	19
Turbulent bedload transport	2.65	100	$\sqrt{\Theta} \in [0.6, 1.1]$	12
Bedload-saltation transition	100	2	$\sqrt{\Theta} \in [0.52, 0.7]$	8
Bedload-saltation transition	100	5	$\sqrt{\Theta} \in [0.4, 0.6]$	5
Bedload-saltation transition	2000	0.5	$\sqrt{\Theta} \in [0.73, 0.9]$	3
Viscous saltation transport	100	10	$\sqrt{\Theta} \in [0.34, 0.64]$	11
Viscous saltation transport	2000	2	$\sqrt{\Theta} \in [0.34, 0.72]$	7
Turbulent saltation transport	100	20	$\sqrt{\Theta} \in [0.35, 0.65]$	4
Turbulent saltation transport	100	50	$\sqrt{\Theta} \in [0.28, 0.31]$	2
Turbulent saltation transport	100	100	$\sqrt{\Theta} \in [0.28, 0.31]$	2
Turbulent saltation transport	2000	5	$\sqrt{\Theta} \in [0.3, 0.6]$	4
Turbulent saltation transport	2000	10	$\sqrt{\Theta} \in [0.35, 0.45]$	2
Gravity flow in ambient air	2000	2	$\alpha \in [51^\circ, 60^\circ]$	4
Gravity flow in ambient air	2000	5	$\alpha \in [48^\circ, 60^\circ]$	5
Gravity flow in ambient air	2000	10	$\alpha \in [42^\circ, 60^\circ]$	7
Gravity flow in ambient air	2000	20	$\alpha \in [36^\circ, 60^\circ]$	9
Gravity flow in ambient air	2000	50	$\alpha \in [33^\circ, 60^\circ]$	10
Gravity flow in ambient air	2000	100	$\alpha \in [30^\circ, 60^\circ]$	11

TABLE S1. Summary of the simulated sediment transport and gravity flow conditions included in Fig. 2.

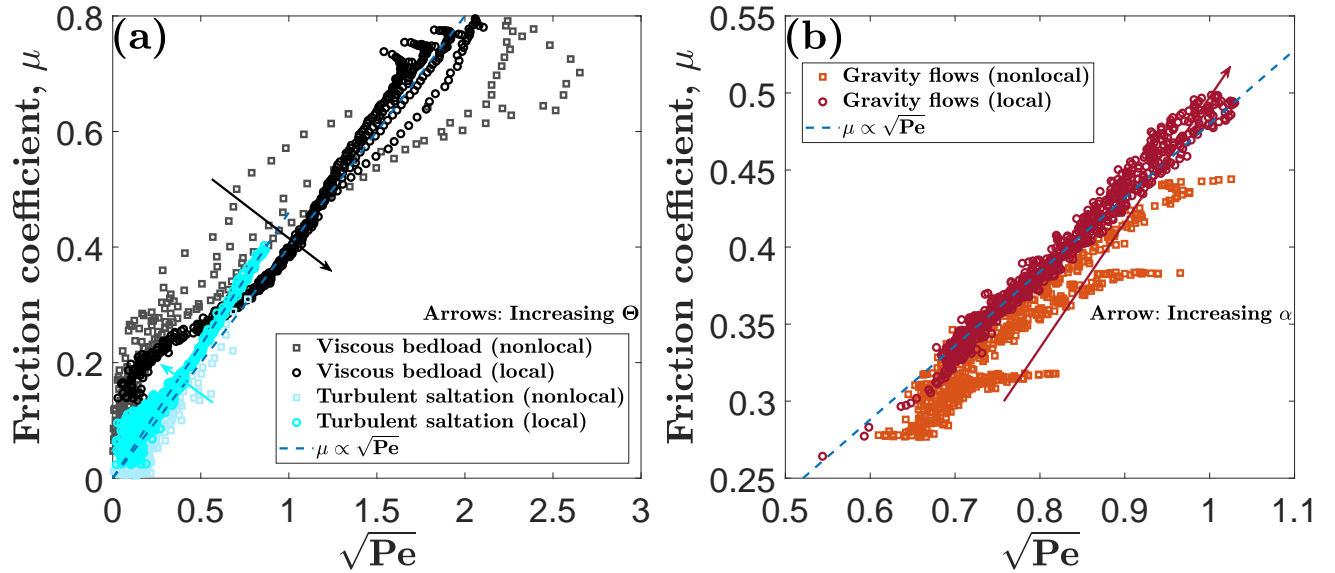


FIG. S1. Friction coefficient μ vs square root of the Péclet number (\sqrt{Pe}) exemplary for (a) viscous bedload transport ($s = 2.65$, $Ga = 5$), turbulent saltation transport ($s = 2000$, $Ga = 5$), and (b) gravity flows submerged in ambient air ($s = 2000$, $Ga = 5$). Symbols correspond to data from our numerical simulations for (a) several Shields numbers Θ and (b) inclination angles α .

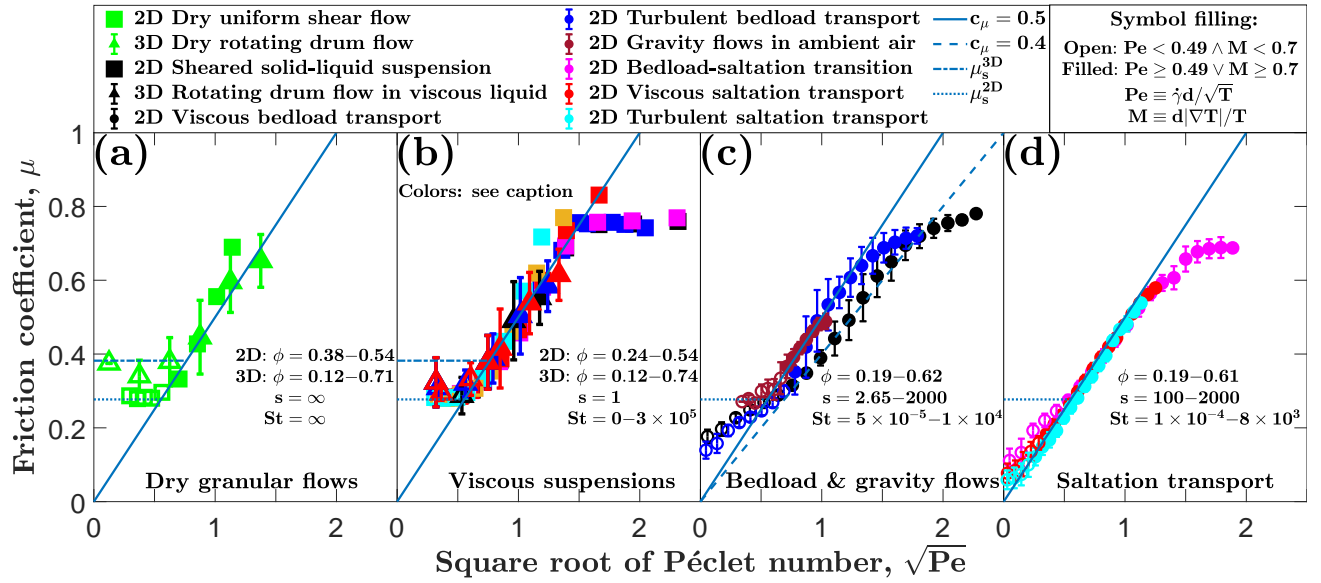


FIG. S2. Mohr-Coulomb friction coefficient μ vs square root of Péclet number (\sqrt{Pe}) for data from discrete element method-based simulations of (a) dry granular flows, (b) viscous suspensions in density-matched liquids, (c) bedload transport and gravity flows, and (d) saltation transport. For the rotating drum flows in (a) and (b) and the sediment transport and gravity flow simulations in (c) and (d), Pe and μ depend on the location within the flow. The value of μ at each location with $\lambda(\phi) < d$ and either $\sqrt{Pe} < 0.7 \wedge M < 0.7$ (open symbols) or $\sqrt{Pe} \geq 0.7 \vee M \geq 0.7$ (filled symbols) is allocated to the corresponding bin of \sqrt{Pe} . Each bin in (a) and (b) consists of data from a single rotating drum or uniform flow simulation, whereas each bin in (c) and (d) consists of data from various simulations of the same regime (Table S1). The mean and standard deviation of μ within each bin are represented by the symbols and their error bars, respectively. For uniform flows, error bars are usually smaller than symbol size and therefore not shown. For the squares in (b), the color order (cyan, orange, red, magenta, blue, black) corresponds to $\eta_f / \sqrt{\rho_p P_{zz} d^2} = [10^{-3}, 10^{-2}, 10^{-1}, 10^0, 10^1, \infty]$. For the triangles in (b), the color order (red, blue, black) corresponds to $\eta_f / (\rho_f \omega d^2) = [1/160, 1/16, 3/16]$.

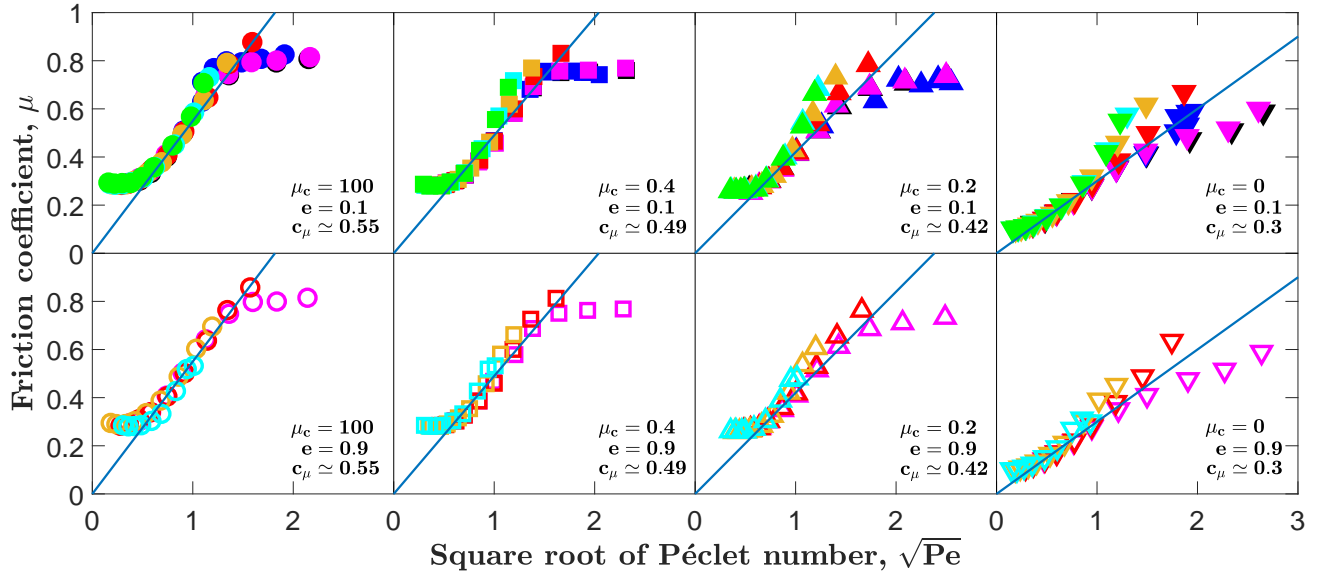


FIG. S3. Mohr-Coulomb friction coefficient μ vs square root of Péclet number (\sqrt{Pe}) for data from discrete element method-based simulations of uniformly sheared particle and suspension flows with varying contact parameters. The color order (green, cyan, orange, red, magenta, blue, black) corresponds to $\eta_f / \sqrt{\rho_f P_{zz} d^2} = [0, 10^{-3}, 10^{-2}, 10^{-1}, 10^0, 10^1, \infty]$.

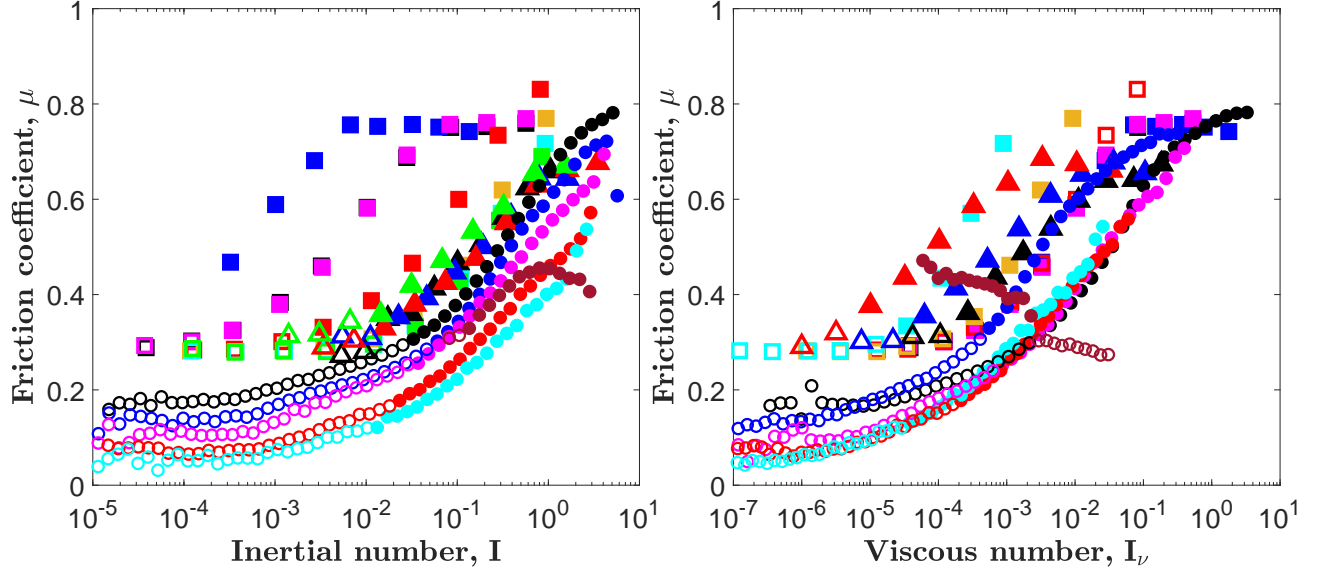


FIG. S4. Mohr-Coulomb friction coefficient μ vs (a) inertial number I and (b) viscous number I_ν for data from discrete element method-based simulations of various granular flows. For rotating drum, sediment transport, and gravity flow simulations, I , I_ν , and μ depend on the location within the flow. The value of μ at each location with $\lambda(\phi) < d$ and either $Pe < 0.49 \wedge M < 0.7$ (open symbols) or $Pe \geq 0.49 \vee M \geq 0.7$ (filled symbols) is allocated to the corresponding bin of I or I_ν . Each bin consists of data from either a single simulation (rotating drum flows) or from various simulations of the same regime (sediment transport and gravity flows, see Table S1). The mean of μ within each bin is represented by the symbols (for standard deviation, see Fig. S2). For the squares, the color order (green, cyan, orange, red, magenta, blue, black) corresponds to $\eta_f/\sqrt{\rho_p P_{zz} d^2} = [0, 10^{-3}, 10^{-2}, 10^{-1}, 10^0, 10^1, \infty]$. For the triangles, the color order (green, red, blue, black) corresponds to $\eta_f/(\rho_f \omega d^2) = [0, 1/160, 1/16, 3/16]$. For symbol legend, see Fig. S2.

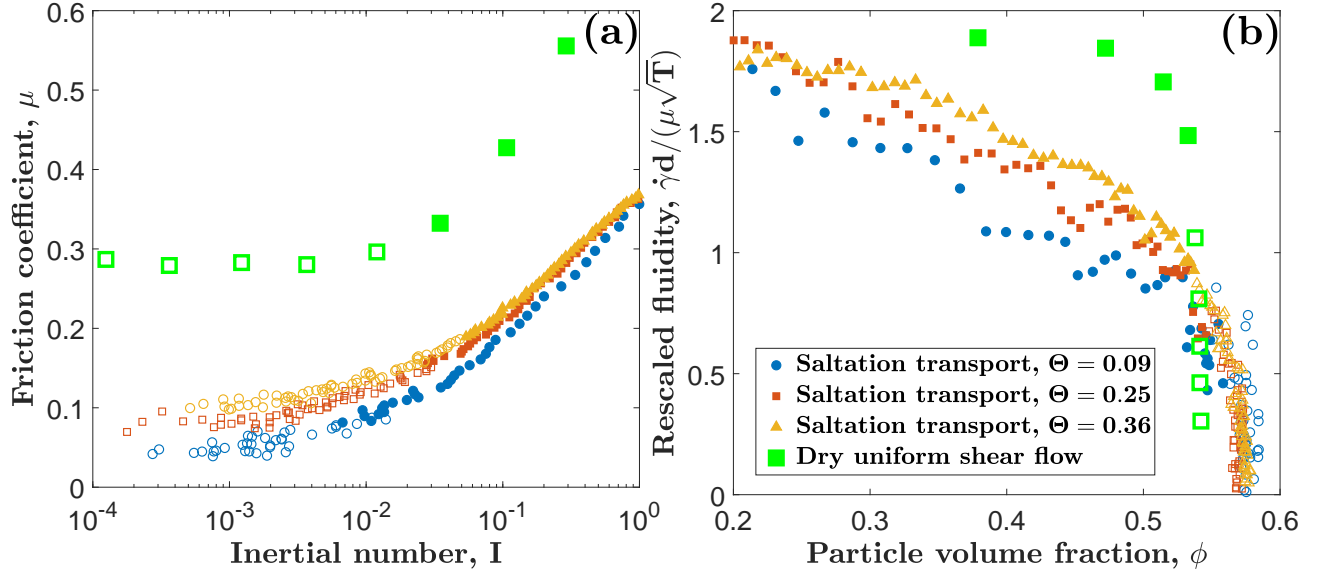


FIG. S5. Failure of viscoplastic rheology and fluidity scaling. (a) Mohr-Coulomb friction coefficient μ vs inertial number I . (b) Rescaled fluidity $[\dot{\gamma}d/(\mu\sqrt{T})]$ vs particle volume fraction ϕ . The small symbols correspond to data from discrete element method-based simulations of turbulent saltation transport ($s = 2000$ and $Ga = 5$) for three different Shields numbers Θ . The large green squares correspond to data from discrete element method-based simulations of dry uniform shear flows. Filled symbols indicate $Pe \geq 0.49 \vee M \geq 0.7$. Open symbols indicate $Pe < 0.49 \wedge M < 0.7$.

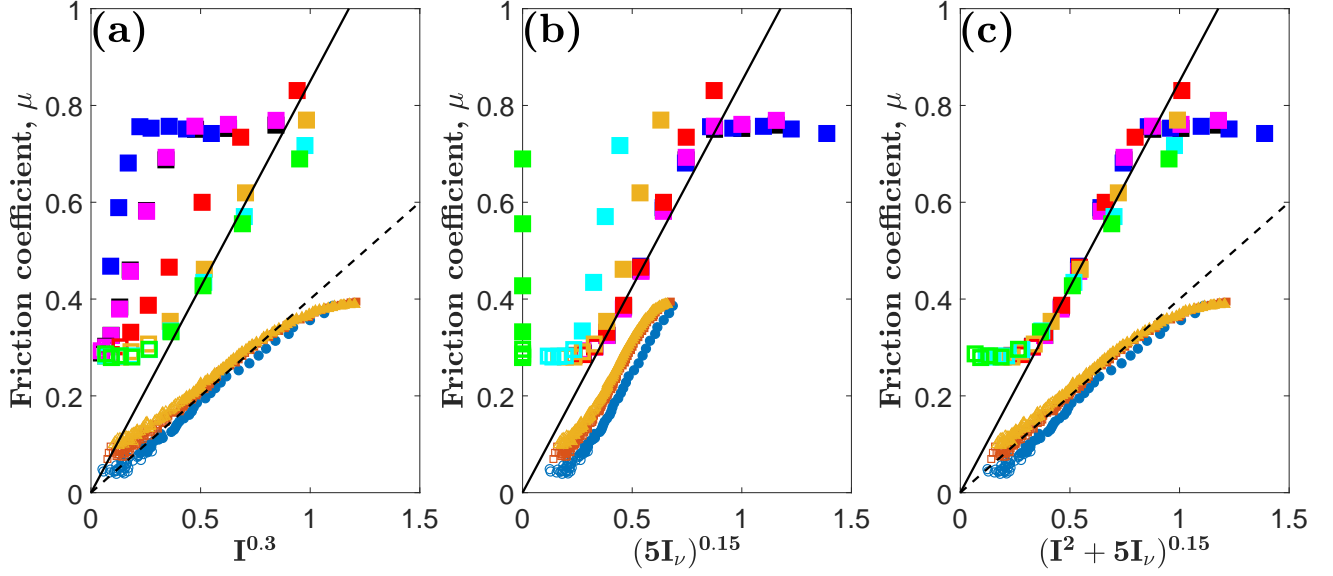


FIG. S6. Failure of viscoinertial rheology. Mohr-Coulomb friction coefficient μ vs (a) $I^{0.3}$, (b) $(5I_\nu)^{0.15}$, and (c) $(I^2 + 5I_\nu)^{0.15}$. The small symbols correspond to data from discrete element method-based simulations of turbulent saltation transport ($s = 2000$ and $\text{Ga} = 5$) for three different Shields numbers Θ . The large squares correspond to data from discrete element method-based simulations of uniformly sheared particle and suspension flows, where the color order (green, cyan, orange, red, magenta, blue, black) indicates $\eta_f/\sqrt{\rho_f P_{zz} d^2} = [0, 10^{-3}, 10^{-2}, 10^{-1}, 10^0, 10^1, \infty]$. Filled symbols indicate $\text{Pe} \geq 0.49 \vee M \geq 0.7$. Open symbols indicate $\text{Pe} < 0.49 \wedge M < 0.7$.

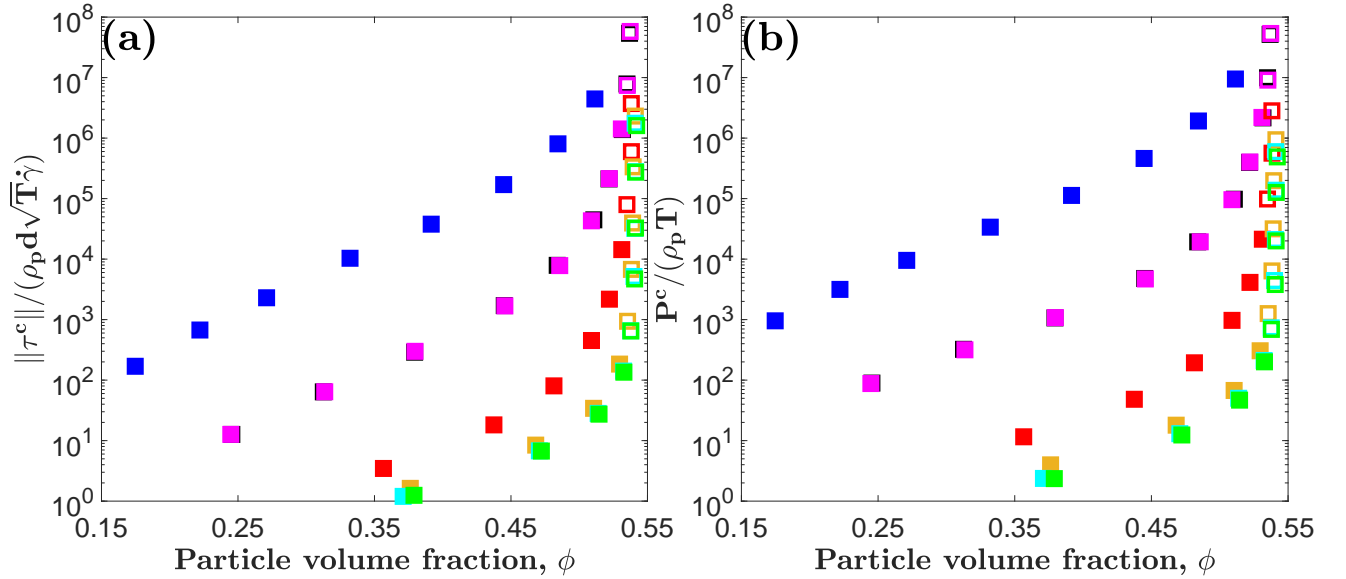


FIG. S7. Failure of extended kinetic theory. (a) Rescaled shear stress $[|\tau^c|/(\rho_p d \sqrt{T} \dot{\gamma})]$ and (b) rescaled pressure $[P^c/(\rho_p T)]$ vs particle volume fraction ϕ for data from discrete element method-based simulations of uniformly sheared particle and suspension flows, where the color order (green, cyan, orange, red, magenta, blue, black) indicates $\eta_f/\sqrt{\rho_f P_{zz} d^2} = [0, 10^{-3}, 10^{-2}, 10^{-1}, 10^0, 10^1, \infty]$. Filled symbols indicate $\text{Pe} \geq 0.49 \vee M \geq 0.7$. Open symbols indicate $\text{Pe} < 0.49 \wedge M < 0.7$.